Title

Imaging human macular pigments with visible light optical coherence tomography and superluminescent diodes.

Journal

Optics Letters, 48(18)

ISSN

0146-9592

Authors

Gupta, Alok K

Meng, Ruoyu

Modi, Yasha S

et al.

Publication Date

2023-09-15

DOI

10.1364/ol.495247

Peer reviewed

HHS Public Access

Author manuscript

Opt Lett. Author manuscript; available in PMC 2024 March 13.

Published in final edited form as:

Opt Lett. 2023 September 15; 48(18): 4737–4740. doi:10.1364/OL.495247.

Imaging human macular pigments with visible light optical coherence tomography and superluminescent diodes

Alok K. Gupta[1,2,3,†], **Ruoyu Meng**[1,3,†], **Yasha S. Modi**[2], **Vivek J. Srinivasan**[1,2,3,*]

[1]Tech4Health Institute, NYU Langone Health, New York, New York, 10010, USA

[2]Department of Ophthalmology, NYU Langone Health, New York, New York, 10016, USA

[3]NYU Tandon School of Engineering, Brooklyn, New York, New York 11201, USA

Abstract

We demonstrate superluminescent diodes (SLDs) for visible light optical coherence tomography (OCT) of the human retina. SLDs are less costly than supercontinuum sources and have lower intrinsic excess noise, enabling imaging closer to the shot noise limit. While single SLDs are not broadband, they provide power concentrated at specific wavelengths relevant to retinal function. As a new, to the best of our knowledge, application, we image human macular pigments (MPs), which are thought to both aid vision and protect against advanced age-related macular degeneration. Using the unique depth-resolved capabilities of OCT, we localize MPs in depth to Henle's fibers beneath the foveal pit in the living human retina. Our approach reduces the cost of visible light OCT to nearly that of near-infrared (NIR) OCT while also providing information about clinically relevant MPs which cannot be measured in the NIR.

Visible light optical coherence tomography (OCT) has shown promise for ultrahigh-resolution imaging [1] and spectroscopy [2] of the retina. Spectral-domain visible light OCT requires sources with high spatial brightness and a relatively broad spectral range. Typical solutions are based on supercontinuum generation from a short pulse [3], which can be expensive, noisy, or both. Though cancelation or balancing approaches can reduce noise [4], these advanced methods are more complex.

Superluminescent diodes (SLDs) are widely used for near-infrared (NIR) OCT. Recently, visible light SLDs were developed for augmented reality. Their high spatial coherence provides sharp displays, and their low temporal coherence reduces speckle [5]. Both traits are desirable for an OCT source. Visible SLDs have been implemented for OCT [6,7], but their performance for retinal imaging was not reported.

The carotenoid macular pigments (MPs) lutein and zeaxanthin (and meso-zeaxanthin) are thought to absorb hazardous blue light, reduce chromatic aberration, scavenge free radicals, and protect against lipid peroxidation. Both protect against advanced age-related macular degeneration (AMD) [8], a leading cause of blindness [9]. Owing to their protective role in

* Vivek.Srinivasan@nyulangone.org .

† These authors contributed equally to this Letter.

Disclosures. The authors declare no conflicts of interest.

AMD, there is immense interest in measuring MPs *in vivo* [10]. Heterochromatic flicker photometry [11,12], multi-wavelength reflectometry [13–16], retinal pigment epithelial lipofuscin autofluorescence [17,18], and Raman spectroscopy [19] have been investigated. Current techniques to measure MPs lack depth resolution and require the extrapolation of a peripheral reference to the fovea, which incorrectly assumes that the only difference between the foveal center and periphery is the presence of MPs. These limitations stand in the way of establishing links between MP concentrations and AMD progression [20,21].

Here, we opportunistically evaluate a 3-SLD combined source (VISIIIBLESRGB, Exalos AG), for retinal visible light OCT. Taking advantage of the spectral intersection of these SLDs with MP absorption, we propose several new methods for OCT imaging and depth localization of MPs.

To quantify MP optical density (O.D.), both spatial and wavelength referencing (normalization) strategies are critical. We considered two ways of spatial referencing. In the eccentricity-referenced approach, inspired by the above MP O.D. methods, we referenced foveal measurements to those at a peripheral eccentricity with an assumed negligible MP O.D. To overcome the major limitations of the eccentricity-referenced approach, we also pursued a depth-referenced approach. In the depth-referenced approach, which leverages the unique capabilities of OCT, we referenced spectra to a more superficial layer to derive MP information. Additionally, we considered two methods of wavelength referencing. In the first method, we referenced blue or green reflectivity to red reflectivity, which is essentially insensitive to MP. In the second method, we used subbands of the green SLD to determine the MP O.D., taking advantage of the sharp increase in MP absorption at green wavelengths.

A visible light OCT system [22] was modified [Fig. 1(a)] to operate with an alignment SLD (red) and a combination of acquisition SLDs (either red and green or red and blue). The different SLDs probe wavelengths with high (blue: 452 nm), moderate (green: 512 nm), or negligible (red: 637 nm) carotenoid absorption [Fig. 1(b)]. A reflective protected silver, 71.8 mm mirror [Fig. 1(a)] was added to the spectrometer to enable the red channel to be focused onto the 4096 pixel camera simultaneously with either the green (G-R mode) or the blue (B-R mode) channel. The mirror essentially extended the spectrometer range, enabling the alignment of subjects with a relatively benign and less bright red SLD prior to image acquisition with shorter wavelengths. Analog outputs modulated SLD drive currents to ensure alignment and acquisition with the appropriate SLDs turned on.

We calibrated the visible light spectrometer as previously described [23] for each SLD using the interferometric phase difference, which provides the relative air wavenumber at each spectrometer pixel, and the known peak wavelength of the manufacturer-provided spectra at a specific SLD current, which determines the air wavenumber at a single pixel [Figs. 2(a)–2(c)]. The mirror in our spectrometer crops the spectrum, as shown by the disagreement in Fig. 2(c). We found that this slight cropping did not significantly impact the image quality.

We next characterized the excess noise of the 3 SLDs independently at 70 kHz by varying the number of photoelectrons during the exposure time [24]. As described previously [24], we modeled the noise as a quadratic function of photoelectron count (pixel gray level)

with 3 coefficients representing camera noise (constant term), shot noise (first-order term), and excess noise (second-order term). The excess noise was determined as a function of wavelength. Using the polynomial fit for each SLD, we predicted the sensitivity relative to the shot noise limit versus the reference arm photoelectron count. All SLDs approached the shot noise limit with more reference counts [Figs. 2(d)–2(f)], in marked contrast to supercontinuum sources [24].

Next, we investigated the sensitivity roll-off and resolution. Note that, since we imaged with only 2 SLDs at once in this study, it was possible to change the sensor alignment [Fig. 1(a)] to independently optimize the sensitivity and roll-off for either red and blue SLDs [Figs. 3(a) and 3(b)] or for red and green SLDs [Figs. 3(c) and 3(d)]. The axial imaging range of the red SLD (Fig. 3) was considerably larger than those of the blue [Figs. 3(a) and 3(b)] and green [Figs. 3(c) and 3(d)] SLDs due to finer sampling in wavenumber at longer wavelengths. Roll-off was only characterized up to the most limiting axial range.

The red SLD (~65 μW) alone was used for alignment. Either red (~65 μW) and blue (~20 μW) or red (~65 μW) and green (~60 μW) SLDs were used simultaneously for imaging. The absolute maximal sensitivity for the green SLD is 91 dB at 30 kHz imaging speed. Power levels are consistent with American National Standards Institute calculations and our IRB protocol, and accounted for the blue light hazard function. Spline interpolation and dispersion compensation [24] were employed in image reconstruction. Protocol 1 acquired 30 repeated images with 840 axial scans separated by 0.006 mm along the slow axis at a 30 kHz axial scan rate. Protocol 2 acquired a raster scan with 490 images with 600 axial scans at a 70 kHz axial scan rate. A lateral range of 4.5 mm was used for both the protocols. Axial motion correction of both channels was performed based on the red frames, followed by intensity averaging. For quantitative O.D., all image intensities were corrected for the noise background bias [23]. Where noted, peripheral referencing was achieved by subtracting a linear fit restricted to >1.25 mm eccentricity. Retinal thickness was taken as the distance from band 2 to the vitreoretinal interface (VRI).

A visual comparison of blue [Fig. 4(a)] and red [Fig. 4(b)] light OCT reveals that the retinal pigment epithelium (RPE)/photoreceptor (PR) complex in the fovea is markedly attenuated at short wavelengths (white arrows), providing clear evidence of MP absorption. To guide quantitative measurements, we adopt a simple model of the OCT intensity, I, which includes backscattering (B), absorption (μ_a), and attenuation due to scattering (μ_s):

$$I = B\exp\left\{-2\int[\mu_s(z') + \mu_a(z')]dz'\right\}. \tag{1}$$

Our goal is to recover μ_a accurately, meaning that we must account for differences in backscattering and attenuation due to scattering. One approach is to perform wavelength referencing:

$$\frac{I_{RPE/PR}(\lambda_B)}{I_{RPE/PR}(\lambda_R)} = \frac{B_{RPE/PR}(\lambda_B)}{B_{RPE/PR}(\lambda_R)}\exp\left\{-2\int\begin{bmatrix}\mu_s(z',\lambda_B) + \mu_a(z',\lambda_B)\\ -\mu_s(z',\lambda_R) - \mu_a(z',\lambda_R)\end{bmatrix}dz'\right\}.$$

(2)

We defined the single-pass blue-red O.D. ratio as

$$\mathrm{O.D.}(\lambda_B, \lambda_R) = \frac{1}{2}\log_{10}\left[\frac{I_{RPE/PR}(\lambda_R)}{I_{RPE/PR}(\lambda_B)}\right] - \mathrm{O.D.}_{periph.}(\lambda_B, \lambda_R),$$

(3)

where λ_B denotes blue and λ_R denotes red. Note that a peripheral reference has been included, which in practice is approximated by a linear fit. This quantity peaked in the foveal pit after peripheral referencing [Fig. 4(c)] with a plausible MP O.D. [25].

Though blue light images [Fig. 4(a)] provided striking visual evidence of MP absorption, the signal-to-noise ratio was poor due to low ocular transmission and low incident power. Also, the normalization wavelengths were far apart, and differing roll-offs may confound measurements. Therefore, we opted not to use blue light subsequently. Turning to the green-red imaging experiments, the 70 kHz raster scan with peripheral referencing mapped the single-pass O.D. ratio, showing MP localization to the foveal pit [Figs. 4(d)–4(f)]. In the fovea, we found that the green-red intensity ratio decreased more steeply in Henle's fiber layer (HFL) than in the ONL [Figs. 4(g)–4(h)]. Assuming that MP absorption mainly accounts for the green-red differences, these results suggest highest MP concentration in HFL [25].

Next, we asked whether the rising edge of MP absorption intersected by the green SLD [Fig. 1(b)] could provide additional information to localize MPs. Two complementary subband analyses of the green SLD were tested. For both analyses, green subband images with an approximately 25 μm FWHM axial tissue resolution were generated by Gaussian shaping. In the first analysis, the background-corrected intensity of the photoreceptor–RPE complex was determined for both the red SLD and the green subbands. After peripheral referencing, the O.D. ratio of each green subband to red showed a peak in the fovea that diminished at longer wavelengths [Fig. 4(i)], as expected from MP absorption spectra [Fig. 1(b)]. The mean peak foveal single-pass MP O.D. was estimated to be 0.095 at 505 nm across 5 subjects. The second analysis aimed to localize MP in depth. For this analysis, we did not normalize to red wavelengths, as scattering may differ between wavelengths. Instead, we essentially used the longer green wavelengths with low MP O.D. as a spectral reference. The subband B-scans were locally averaged over 100 μm in the transverse direction to reduce noise. The VRI spectrum outside the fovea was the spatial reference. The intensity (I) at depth z as a function of wavelength (λ) and normalized to the reference intensity is

$$\frac{I(z,\lambda)}{I(z_{VRI},\lambda)} = \frac{B(z,\lambda)}{B(z_{VRI},\lambda)}\exp\left\{-2\int_{z_{VRI}}^{z}[\mu_s(z')+\mu_a(z',\lambda)]dz'\right\}.$$

(4)

The backscattering (B) ratio, defined as R_B, and the attenuation coefficient due to scattering, μ_s, are assumed not to depend on λ within the relatively small green SLD range. The depth-resolved single-pass O.D. is

$$\mathrm{O.D.}(z,\lambda) = -\frac{1}{2}\log_{10}\left[\frac{I(z,\lambda)}{I(z_{VRI},\lambda)}\right] = -\frac{1}{2}\log_{10}[R_B(z)] + \log_{10}(e)\int_{z_{VRI}}^{z}[\mu_s(z') + \mu_a(z',\lambda)]dz'. \tag{5}$$

With the above assumptions, the λ dependence of Eq. (5) is fully attributable to μ_a, and thus the MP absorption can be recovered by spectral fitting. The next question is which MP spectrum to use. The exact proportion of lutein and zeaxanthin is unknown *in vivo* and varies with eccentricity. There are also discrepancies among published MP spectra [21]. Therefore, we adopted a data-driven algorithm to learn the experimental MP absorption spectra. Basically, we began by assuming an MP absorption spectrum $A(\lambda)$ that varied linearly with wavelength, fitted the data at each image pixel assuming that the O.D. is approximated with coefficients C_0 and C_1 [Eq. (6)], and then updated our assumed MP absorption spectrum $A(\lambda)$ as the average of the O.D. at high R^2 (>0.6) locations

$$\mathrm{O.D.}(z,\lambda) \approx C_0(z) + C_1(z)A(\lambda). \tag{6}$$

We repeated the fitting procedure with the new MP absorption spectrum $A(\lambda)$, continuing for 8 iterations until $A(\lambda)$ converged. The shape that was learned from the data agrees qualitatively with the absorption coefficient in Fig. 1(b), further reassuring us that the absorbance $A(\lambda)$ is due to MP. We recognize that C_1, shown in Fig. 5(b), represents the cumulative MP content that is traversed up to depth z,

$$C_1(z) \approx \log_{10}(e)\int_{z_{VRI}}^{z}\mu_a(z',\lambda)dz'/A(\lambda). \tag{7}$$

The absorption coefficient is given as $\mu_a(z,\lambda) = \varepsilon(\lambda)\rho(z)$, where ε is the extinction and ρ is the concentration. Figure 5(b) presents the cumulative MP absorption. The derivative dC_1/dz should yield the local MP concentration [Fig. 5(c)]:

$$\frac{dC_1}{dz} \approx \frac{\log_{10}(e)\mu_a(z,\lambda)}{A(\lambda)} = \frac{\log_{10}(e)\varepsilon(\lambda)\rho(z)}{A(\lambda)} \propto \rho(z), \tag{8}$$

where the last step in Eq. (8) assumes that our inferred absorbance $A(\lambda)$ is proportional to $\varepsilon(\lambda)$. As shown in Fig. 5(c), MPs are found to be mainly distributed in the foveal center transversely and the HFL axially, in agreement with prior work [21]. We hypothesize that detecting trace MP levels in other layers will require improvements in the sensitivity of our

system and algorithm. Equation (8) is clearly a depth-referenced approach as it examines local changes with depth. However, while Eq. (8) does not depend explicitly on the choice of spatial reference, there is an implicit dependence since the absorbance spectrum $A(\lambda)$ does, owing to the above-described data-driven approach used to determine the MP absorption.

In summary, we have presented novel approaches to investigate MPs with SLD-based visible light OCT. The approach highlighted in Fig. 5 provides, to the best of our knowledge, the first depth localization of MPs in the living eye. Topics of ongoing investigation include optimal wavelengths for MP O.D., the detection of MPs in the inner plexiform layer, a rigorous comparison of referencing techniques, and even possibly distinguishing lutein from zeaxanthin.

Funding.

National Institutes of Health (R01EY031469, R01NS094681); Research to Prevent Blindness.

Data availability.

Data underlying the results presented in this paper are not publicly available at this time but may be obtained from the authors upon reasonable request.

REFERENCES

1. Povazay B, Bizheva K, Unterhuber A, Hermann B, Sattmann H, Fercher AF, Drexler W, Apolonski A, Wadsworth WJ, Knight JC, Russell PSJ, Vetterlein M, and Scherzer E, Opt. Lett 27, 1800 (2002). [PubMed: 18033368]
2. Wang J, Baker A, Subramanian ML, Siegel NH, Chen X, Ness S, and Yi J, Exp. Biol. Med 247, 377 (2022).
3. Brown WJ, Kim S, and Wax A, J. Opt. Soc. Am. A 31, 2703 (2014).
4. Kho AM and Srinivasan VJ, Opt. Express 29, 42037 (2021).
5. Deng Y and Chu D, Sci. Rep 7, 5893 (2017). [PubMed: 28724961]
6. Lichtenegger A, Salas M, Sing A, Duelk M, Licandro R, Gesperger J, Baumann B, Drexler W, and Leitgeb RA, Biomed. Opt. Express 12, 6780 (2021). [PubMed: 34858680]
7. Khan S, Neuhaus K, Thaware O, Ni S, Ju MJ, Redd T, Huang D, and Jian Y, Biomed. Opt. Express 13, 5004 (2022). [PubMed: 36187260]
8. Beatty S, Boulton M, Henson D, Koh HH, and Murray IJ, Br. J. Ophthalmol 83, 867 (1999). [PubMed: 10381676]
9. Age-Related Eye Disease Study Research Group, Arch. Ophthalmol 125, 1225 (2007). [PubMed: 17846363]
10. Howells O, Eperjesi F, and Bartlett H, Graefes Arch. Clin. Exp. Ophthalmol 249, 315 (2011). [PubMed: 21221629]
11. Hammond BR Jr., Curran-Celentano J, Judd S, Fuld K, Krinsky NI, Wooten BR, and Snodderly DM, Vision Res 36, 2001 (1996). [PubMed: 8759440]
12. Landrum JT, Bone RA, Joa H, Kilburn MD, Moore LL, and Sprague KE, Exp. Eye Res 65, 57 (1997). [PubMed: 9237865]
13. Gellermann W and Bernstein PS, J. Biomed. Opt 9, 75 (2004). [PubMed: 14715058]
14. Delori FC and Burns SA, J. Opt. Soc. Am. A 13, 215 (1996).
15. Berendschot TT, Goldbohm RA, Klopping WA, van de Kraats J, van Norel J, and van Norren D, Invest. Ophthalmol. Vis. Sci 47, 709 (2006). [PubMed: 16431971]
16. Loughman J, Scanlon G, Nolan JM, O'Dwyer V, and Beatty S, Acta. Ophthalmol 90, e90 (2012). [PubMed: 22067014]

17. Delori FC, Dorey CK, Staurenghi G, Arend O, Goger DG, and Weiter JJ, Invest. Ophthalmol. Vis. Sci 36, 718 (1995). [PubMed: 7890502]
18. Delori FC, Arch. Biochem. Biophys 430, 156 (2004). [PubMed: 15369813]
19. Bernstein PS, Yoshida MD, Katz NB, McClane RW, and Gellermann W, Invest. Ophthalmol. Vis. Sci 39, 2003 (1998). [PubMed: 9761278]
20. Beatty S, van Kuijk FJGM, and Chakravarthy U, Invest. Ophthalmol. Vis. Sci 49, 843 (2008). [PubMed: 18326700]
21. Bernstein PS, Delori FC, Richer S, van Kuijk FJ, and Wenzel AJ, Vision Res 50, 716 (2010). [PubMed: 19854211]
22. Srinivasan VJ, Kho AM, and Chauhan P, Trans. Vis. Sci. Tech 11, 3 (2022).
23. Chong SP, Merkle CW, Leahy C, Radhakrishnan H, and Srinivasan VJ, Biomed. Opt. Express 6, 1429 (2015). [PubMed: 25909026]
24. Chong SP, Bernucci M, Radhakrishnan H, and Srinivasan VJ, Biomed. Opt. Express 8, 323 (2017). [PubMed: 28101421]
25. Kar D, Clark ME, Swain TA, McGwin G Jr., Crosson JN, Owsley C, Sloan KR, and Curcio CA, Invest. Ophthalmol. Visual Sci 61, 46 (2020).

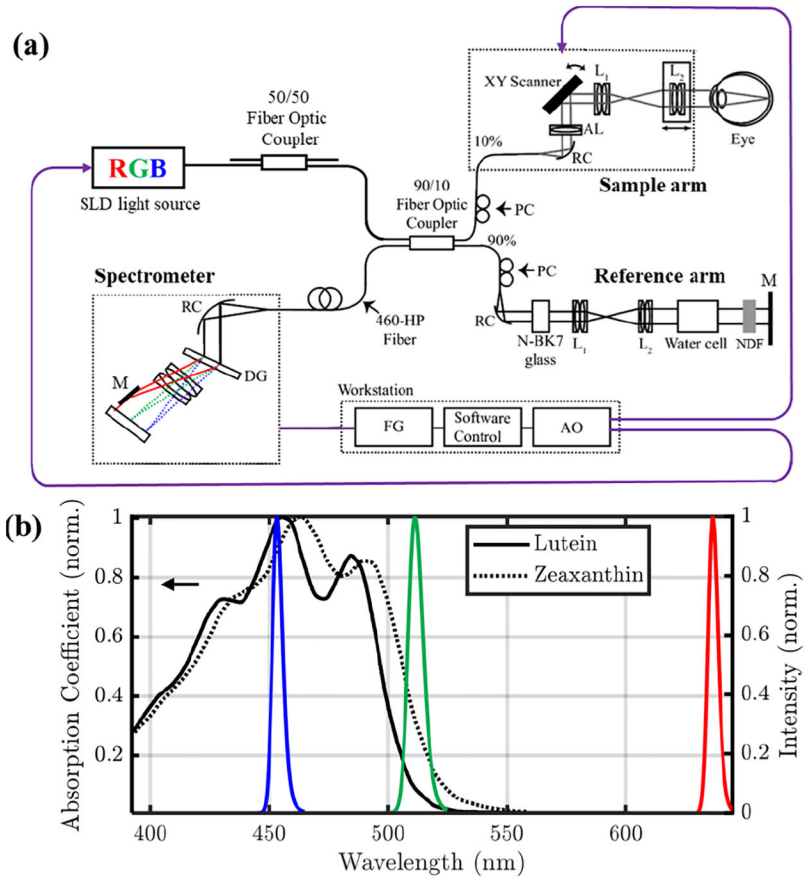

Fig. 1.

(a) Visible light OCT system for *in vivo* human retinal imaging which operates with an alignment SLD (red) and a combination of acquisition SLDs (either red and green or red and blue). PC: polarization controller; RC: reflective collimator; AL: achromatizing lens; L: lens; NDF: neutral density filter; M: mirror, FG: frame grabber, AO: analog output; DG: diffractive grating. A 50/50 coupler after the source provides attenuation. (b) Normalized carotenoid absorption [21] with SLD spectra. While all SLDs are shown, only two at a time were used for imaging.

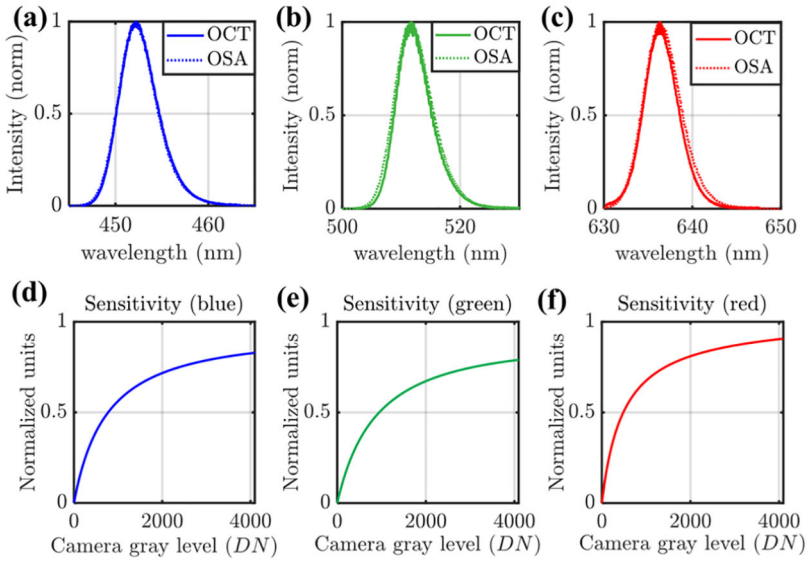

Fig. 2.

(a)–(c) Comparison of spectra measured by an optical spectrum analyzer (OSA) with those measured by our OCT spectrometer [Fig. 1(a)]. (d)–(f) Sensitivity relative to the shot noise limit versus the reference gray level at 70 kHz. Maximal sensitivity is attained by nearly saturating the reference arm.

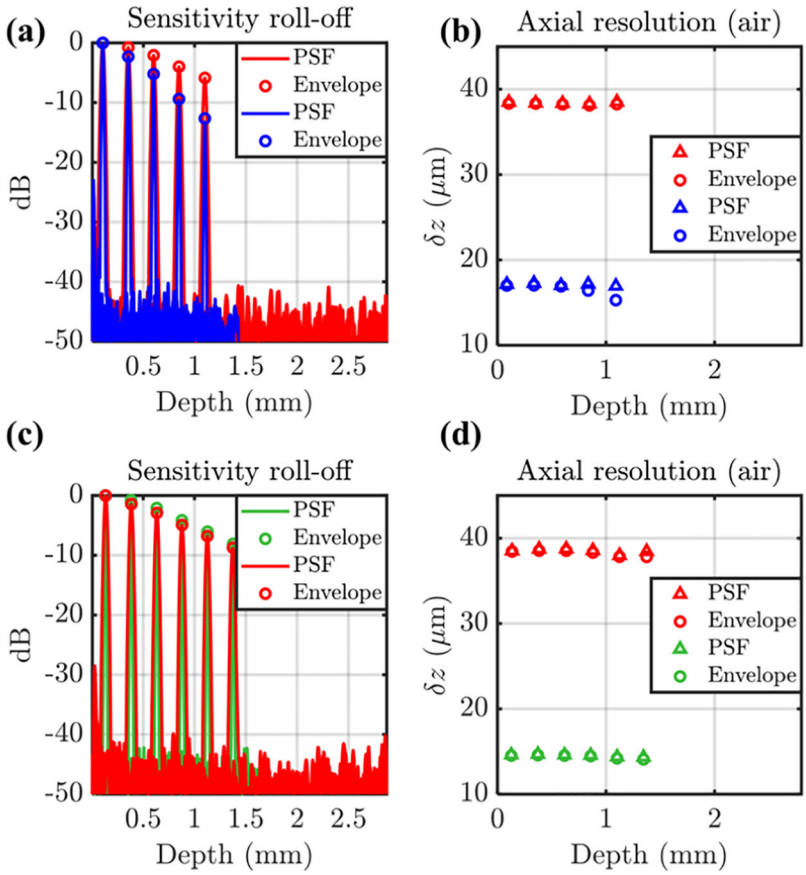

Fig. 3.

(a) Sensitivity roll-off versus depth in air for (a) the B-R mode and (c) the G-R mode, and axial resolution versus depth in air for (b) the B-R mode and (d) the G-R mode.

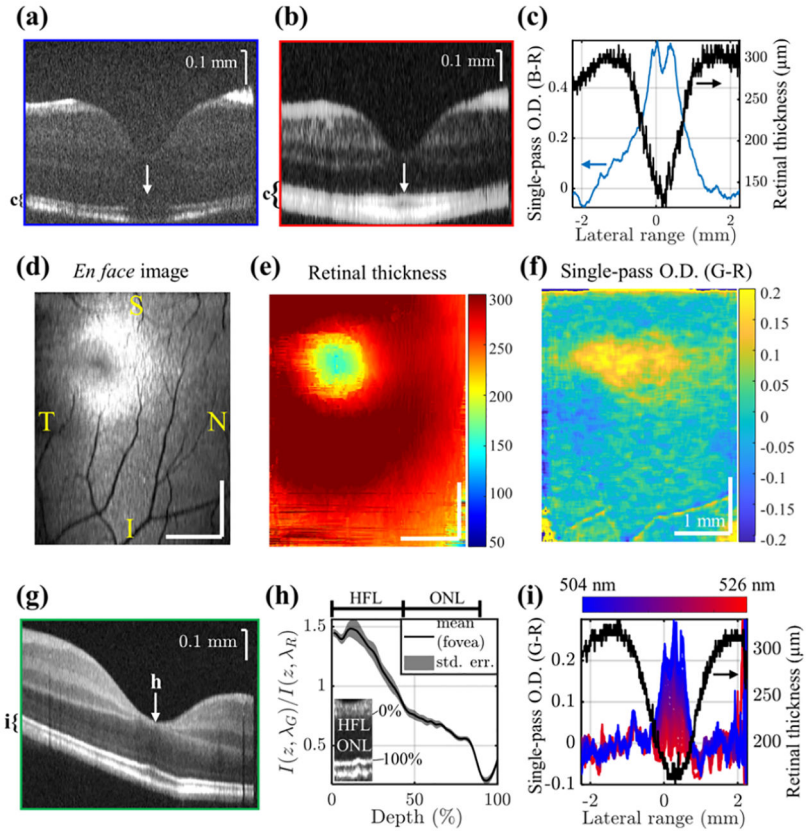

Fig. 4.

(a) Blue and (b) red OCT images. (c) Single-pass blue-red O.D. ratio with peripheral referencing (protocol 1). (d)–(f) *En face* image, retinal thickness, and single-pass green-red O.D. ratio (protocol 2). (g) Green OCT image, (h) depth-resolved green-red intensity ratio within Henle's fiber layer (HFL) and the outer nuclear layer (ONL), and (i) single-pass green subband-red O.D. ratio with peripheral referencing (protocol 1). T: temporal; S: superior; N: nasal; I: inferior. Differences in image detail between (a), (b), and (g) are consistent with the axial resolutions [Fig. 3(b) and 3(d)].

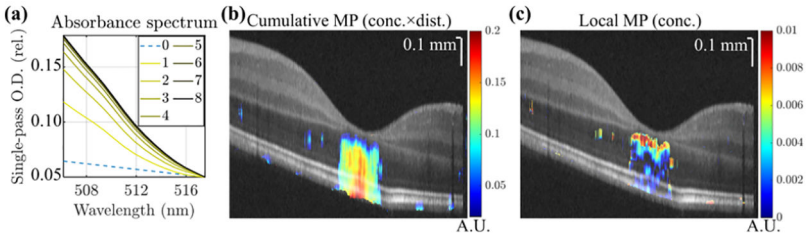

Fig. 5.

Depth-referenced analysis of the green SLD spectrum (protocol 1). (a) MP absorbance versus iteration number for the data-driven approach shows a transition from a linear spectrum to a concave-up spectrum, in agreement with Fig. 1(b). (b) Cumulative MP absorption [Eq. (6)]. (c) Local MP concentration [Eq. (8)].